Journal of Hydroscience and Hydraulic Engineering
Vol. 23, No.2 November, 2005, 27-42

# THREE-DIMENSIONAL NUMERICAL SIMULATION OF PARTICLE CLOUDS FOR OPEN WATER SEDIMENT DISPOSAL

By

Jaswant SINGH, Juichiro AKIYAMA and Mirei SHIGE-EDA
Department of Civil Engineering, Kyushu Institute of Technology,
Sensuicho 1-1, Tobata, Kitakyushu 804-8550, Japan.

## SYNOPSIS

A three-dimensional numerical model for simulating the motion of particle clouds for an open water sediment disposal was developed. The model is based on Large Eddy Simulation (LES) and assumes that the discrete particles can be represented by a continuous field of density difference and Boussinesq approximations. A sensitivity analysis on the model constants, namely Smagorinsky constant and Schmidt number, was performed, and suitable values of these were estimated. Then the model was tested against reported experimental data of two-dimensional (2D) as well as axisymmetric particle clouds. Furthermore, the model was applied to a prototype scale situation to investigate the effects of the ratio of initial length to initial width of suspension and the ambient depth on the subsequent behavior of the cloud.

## INTRODUCTION

Dredge material, soil or industrial waste is often dumped into the ocean for the purpose of artificial land reclamation, and for waste disposal. To predict the amount and the extent of turbidity in such projects is of great importance in evaluating their impact on marine environment and in planning such counter-measures as turbidity fence for preventing diffusion of turbidity.

When a large amount of particles is instantaneously released into quiescent water with finite depth, a turbulent particle cloud is formed. The cloud falls through the ambient water under its own gravity force, entraining ambient water. In this study, this falling motion of the cloud is referred to as "the falling stage". After impingement on the bottom, the cloud spreads over the bottom in the form of a gravity current. Such motion of the cloud is referred to as "the spreading stage".

The motion and diffusion of the particle cloud in the falling stage has been extensively investigated by other researchers. For instance, Akiyama et al. (1) conducted experiments on two-dimensional (2D) turbulent dense thermals and developed an integral model to predict such flow characteristics as half width, velocity and effective gravity force. Akiyama et al. (3) extended the model for particle clouds. Noh and Fernando (15) conducted experiments on two-dimensional particle clouds and developed a relationship for the critical depth at which the two-dimensional cloud transits into swarm phase. Axisymmetric clouds have been investigated in many studies, to mention a few are Tamai et al..(20), Baines and Hopfinger (4), Buhler and Papantoniou (5), Bush et al. (6), Maxworthy (12), Rohimipour and Wilkinson (16), Ruggaber (17). In all the above studies, the analysis is essentially based on a thermal theory. Numerical investigations are also reported on the subject. For instance, Li and Zang (11) developed a three-dimensional (3D) model to investigate line and axisymmetric clouds by means of a characteristic based scheme with flux limiters. But their model over-estimated the nominal width of line cloud. Li (10) studied the clouds numerically using a three-dimensional model in which Prandtl mixing length model was used to calculate eddy viscosity. For smaller particle sizes (0.15 ~ 0.30mm), the model reproduced half width and velocity reasonably well, but for the particles of larger diameter

(0.6~1.18 mm), the model failed to simulate the half width and velocity of the cloud. Nadaoka et al. (14) performed numerical simulation of particle plume with Grid Averaged Lagrangian (GAL) model using Large Eddy Simulation (LES).

As for the spreading stage, Akiyama et al. (3) observed that the two-dimensional particle cloud impinged on the bottom in thermal phase, carries the particle away from the point of impingement in the form of a gravity current, while a cloud impinged in the swarm phase does not form a gravity current and the particles settle down near the point of impingement. Jiang et al. (8) developed two-dimensional numerical model and verified the model with experimental results of particle cloud from the falling to spreading stage. Tamai and Muraoka (19) qualitatively investigated turbidity transport produced by direct dumping of soil, by means of the k-ε model. Ying et al. (21) studied two-dimensional particle clouds from the falling stage to the spreading stage experimentally and numerically. Akiyama et al. (2) investigated the motion and diffusion of two-dimensional particle clouds on a horizontal bed with and without a turbidity fence, using LES.

In this study, a three-dimensional numerical model is developed using LES for simulating the motion of the particle cloud produced by direct dumping of sediments into the quiescent water with finite depth. A sensitivity analysis of the model constants, namely Smagorinsky constant and Schmidt number, is carried out and suitable values of these are estimated. Then the model is verified against the experimental data of two-dimensional particle cloud from the falling to the spreading stage, reported by Akiyama et al. (2) and against the experimental data of axisymmetric particle cloud in the falling stage reported by Ruggaber (17). Since the ratio of the initial length to the initial width of the suspension $\zeta$ and ambient water depth $h$ are important parameters in the motion of cloud and diffusion of particles, the effects of $\zeta$ and $h$ on the front height, the intrusion distance, the front propagating speed and the effective gravity force of deposited particles are also investigated under prototype scale conditions.

## MODEL DEVELOPMENT

A particle cloud is generated by direct dumping of the large amount of particles into ambient water and hence use of Lagrangian approach (Snider (18)), in which individual particle is tracked, is not suitable for modeling the considering flow. For this reason, one equation model is used in this study. The particle phase is treated as a fluid phase, and the drift velocity between fluid and particles is assumed to be the settling velocity of the particles, and the Boussinesq approximation is used.

The governing equations include grid filtered three-dimensional, incompressible continuity equation, Navier-Stokes equations and a mass transport equation. The flow variables of the Navier-Stokes equations are decomposed into large-scale, that is, resolvable part and a sub-grid-scale, i.e., unresolved part. The large-scale (or resolvable) equations of motion are obtained by filtering of governing equations using a grid filter function. The filtered equations are expressed as follows:

$$\frac{\partial U_l}{\partial x_l} = 0 \tag{1}$$

$$\frac{\partial U_l}{\partial t} + U_m \frac{\partial U_l}{\partial x_m} = -\frac{1}{\rho_a}\frac{\partial P}{\partial x_l} + \nu \frac{\partial^2 U_l}{\partial x_m^2} + \frac{\partial}{\partial x_m}\left(-\overline{u_l' u_m'}\right) + g_l \frac{\Delta\rho}{\rho_a} \tag{2}$$

$$\frac{\partial C}{\partial t} + \left(U_l + V_{sl}\right)\frac{\partial C}{\partial x_l} = \frac{\partial}{\partial x_l}\left(\frac{\nu}{S_c}\frac{\partial C}{\partial x_l} - \overline{u_l' c'}\right) \tag{3}$$

where $l$, $m$ =1,2,3, $U_l$ = resolved velocity component in the $x_l$ direction, $P$ = pressure in excess of the hydrostatic pressure at reference density, $\Delta\rho$ = density difference between suspension fluid $\rho$ and ambient water $\rho_a$, $\nu$ = kinematic viscosity, $g$ = acceleration due to gravity, $u_l'$ = unresolved component

of velocity, $C$ = volumetric concentration of suspension, $S_c$ = Schmidt number, $c'$ = unresolved part of concentration and $V_s$ = settling velocity of a particle which is computed by Rubey's equation given as:

$$V_s = \sqrt{sgd}\left(\sqrt{\frac{2}{3}+\frac{36\nu^2}{sgd^3}}-\sqrt{\frac{36\nu^2}{sgd^3}}\right) \tag{4}$$

where $s$ = submerged specific gravity of a particle, $d$ = particle diameter.

Sub-grid or unresolved terms that appear in the momentum and mass conservation equation are of the form $\overline{u_l'u_m'}$, which is sub-grid correlation terms between unresolved components of velocities due to the grid filtering, and $\overline{u_l'c'}$, which is sub-grid correlation terms between unresolved velocity component and unresolved concentration component and can be expressed as follows;

$$-\overline{u_l'u_m'} = \nu_t\left(\frac{\partial U_l}{\partial x_m}+\frac{\partial U_m}{\partial x_l}\right)-\frac{2}{3}k\delta_{lm} \tag{5}$$

where $\nu_t$ = sub-grid scale eddy viscosity, $k$ = turbulent kinetic energy, $\delta_{lm}$ = kronecker delta function. The last term in Eq. 5 represents the normal stresses and can be absorbed in the pressure terms of the momentum equations. Sub-grid correlation term $\overline{u_l'c'}$ in Eq. 3 is generally expressed as follows;

$$-\overline{u_l'c'} = \frac{\nu_t}{S_{ct}}\frac{\partial C}{\partial x_l} \tag{6}$$

Where $S_{ct}$ is turbulent Schmidt number. In LES, the unresolved small-scale turbulence is treated by a sub-grid scale (SGS) model. In this study, the Smagorinsky model is adopted as a SGS model. The sub-grid scale eddy viscosity $\nu_t$ is calculated by using the modified Smagorinsky model, where it is assumed that the sub-grid turbulent production includes a buoyancy term (Ying et al. (21)). Therefore,

$$\nu_t = (C_s\Delta)^2\left(\left|\overline{S}\right|^2-\frac{g_l}{\rho S_{ct}}\frac{\partial\Delta\rho}{\partial x_l}\right)^{1/2} \tag{7}$$

where $\Delta$ = filter width and $C_s$ = Smagorinsky constant. The magnitude of large-scale strain $\left|\overline{S}\right|$ is given by

$$\left|\overline{S}\right| = \left(2\overline{S}_{lm}\overline{S}_{lm}\right)^{1/2} \tag{8}$$

$$\overline{S}_{lm} = \frac{1}{2}\left(\frac{\partial U_l}{\partial x_m}+\frac{\partial U_m}{\partial x_l}\right) \tag{9}$$

## SOLUTION METHODOLOGY

Using the operator splitting approach, Eq. 2 can be split into advection-diffusion equation (Eq.10) and pressure equation (Eq.11) after every time step.

$$\frac{\partial U_l}{\partial t}+U_m\frac{\partial U_l}{\partial x_m} = \frac{\partial}{\partial x_m}\left((\nu+\nu_t)\overline{S}_{lm}\right) \tag{10}$$

$$\frac{\partial U_l}{\partial t} = -\frac{1}{\rho_a}\frac{\partial P}{\partial x_l}+g_l\frac{\Delta\rho}{\rho_a} \tag{11}$$

Eq.10 is discretized by means of a fourth order accurate Compact Finite Difference (CFD) scheme (Lele (9)) as follows:

$$U_{1_{i,j,k}}^{n+1/2} = U_{1i,j,k}^{n} - \Delta t \frac{U_{1_{i,j,k}}^{n}}{12\Delta x}\left(U_{1_{i-2,j,k}}^{n} - 8U_{1_{i-1,j,k}}^{n} + 8U_{1_{i+1,j,k}}^{n} - U_{1_{i+1,j,k}}^{n}\right) - \Delta t \frac{U_{1_{i,j,k}}^{n}}{12\Delta y}\left(U_{1_{i,j-2,k}}^{n} - 8U_{1_{i,j-1,k}}^{n} + 8U_{1_{i,j+1,k}}^{n} - U_{1_{i,j+1,k}}^{n}\right)$$
$$- \frac{U_{1_{i,j,k}}^{n}}{12\Delta z}\left(U_{1_{i,j,k-2}}^{n} - 8U_{1_{i,j,k-1}}^{n} + 8U_{1_{i,j,k+1}}^{n} - U_{1_{i,j,k+1}}^{n}\right)$$
$$+ \frac{\left(\nu + \nu_{t_{i,j,k}}\right)\Delta t}{12\Delta x^2}\left(-U_{1_{i-2,j,k}}^{n} + 16U_{1_{i-1,j,k}}^{n} - 30U_{1_{i,j,k}}^{n} + 16U_{1_{i+1,j,k}}^{n} - U_{1_{i+2,j,k}}^{n}\right)$$
$$+ \frac{\left(\nu + \nu_{t_{i,j,k}}\right)\Delta t}{12\Delta y^2}\left(-U_{1_{i,j-2,k}}^{n} + 16U_{1_{i,j-1,k}}^{n} - 30U_{1_{i,j,k}}^{n} + 16U_{1_{i,j+1,k}}^{n} - U_{1_{i,j+2,k}}^{n}\right) +$$
$$+ \frac{\left(\nu + \nu_{t_{i,j,k}}\right)\Delta t}{12\Delta z^2}\left(-U_{1_{i,j,k-2}}^{n} + 16U_{1_{i,j,k-1}}^{n} - 30U_{1_{i,j,k}}^{n} + 16U_{1_{i,j,k+1}}^{n} - U_{1_{i,j,k+2}}^{n}\right) \qquad (12)$$

Other equations for $U_2$ and $U_3$ can be discretized in the similar way. The pressure is computed by the Poisson type equation, derived from algebraic manipulations of Eqs. 1 and 11. Pressure equation being an equilibrium problem can also be solved as an unsteady problem whose steady state solution is sought. Thus, the derived poison type pressure equation is as follows:

$$\frac{\partial^2 P}{\partial x_l^2} - \frac{\rho_a}{\partial t}\left(\frac{\partial U_l}{\partial x_l}^{(n+1/2)\Delta t}\right) - g_l \frac{\partial \Delta\rho}{\partial x_l} = 0 \qquad (13)$$

Eq.13 is discretized by means of the central difference method and is solved by means of the Successive Over Relaxation (SOR) method.

$$\frac{\Delta t}{\Delta x^2}(P_{i-1,j,k}^{n+1} - 2P_{i,j,k}^{n+1} + P_{i+1,j,k}^{n+1}) + \frac{\Delta t}{\Delta y^2}(P_{i,j-1,k}^{n+1} - 2P_{i,j,k}^{n+1} + P_{i+1,j,k}^{n+1}) + \frac{\Delta t}{\Delta z^2}(P_{i,j,k-1}^{n+1} - 2P_{i,j,k}^{n+1} + P_{i,j,k+1}^{n+1}) =$$
$$\rho_{a,i,j,k}\left(\frac{U_{1_{i-1,j,k}}^{n+1/2} - U_{1_{i+1,j,k}}^{n+1/2}}{2\Delta x} + \frac{U_{2_{i,j-1,k}}^{n+1/2} - U_{2_{i,j+1,k}}^{n+1/2}}{2\Delta y} + \frac{U_{3_{i,j,k-1}}^{n+1/2} - U_{3_{i,j,k+1}}^{n+1/2}}{2\Delta z}\right)$$
$$+ g_1 \frac{\Delta t}{2\Delta x}\left(\Delta\rho_{i-1,j,k}^{n} - \Delta\rho_{i+1,j,k}^{n}\right) + g_2 \frac{\Delta t}{2\Delta x}\left(\Delta\rho_{i,j-1,k}^{n} - \Delta\rho_{i,j+1,k}^{n}\right) + g_3 \frac{\Delta t}{2\Delta x}\left(\Delta\rho_{i,j,k-1}^{n} - \Delta\rho_{i,j,k+1}^{n}\right) \qquad (14)$$

Inserting Eq.6 into Eq.3, we get

$$\frac{\partial C}{\partial t} + (U_l + V_{si})\frac{\partial C}{\partial x_i} = \frac{1}{S_{ct}}\frac{\partial}{\partial x_l}\left((\nu + \nu_t)\frac{\partial C}{\partial x_l}\right) \qquad (15)$$

Eq.15 is also discretized by means of the CFD scheme in the same manner as Eq.12. Solving Eq.12, $U_l$ is computed at intermediate time step (n+1/2) using Crank-Nicholson method, without inclusion of pressure terms. Using these velocities, Poisson equation Eq.14 is solved by using the SOR method to calculate pressure $P^{n+1}$ at next time step. If the velocity and pressure are known as above, Eq. 11 can be solved for velocities $U_l$ at the next time level. Mass transport equation Eq.15 is solved to

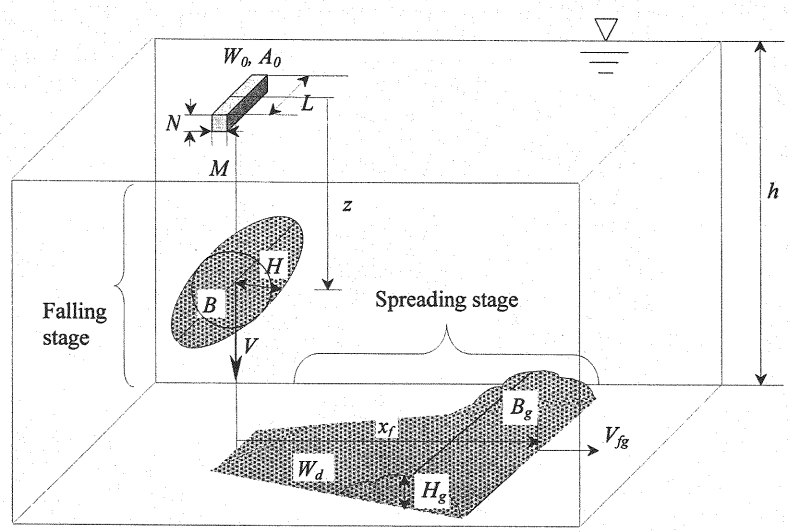


**Fig. 1** Definition sketch showing the motion of particle cloud from the falling to spreading stage.

update excess density. This process is repeated for reaching to next time level.

The imposed boundary conditions for velocity, pressure and concentration are $U_\tau = 0$ and $U_n = 0$, for bottom and side boundaries, $\partial U_\tau/\partial n = 0$ and $U_n = 0$, for top boundary, $\partial P/\partial n = 0$ and $\partial C/\partial n = 0$, for all boundaries, where $\tau$ and $n$ denote direction tangential and normal to boundary respectively. The free water surface is treated as a rigid boundary in the computations. In the spreading stage an additional boundary condition is imposed to take into account the deposition of particles from the flow onto the bed. The net deposition rate $D$ is estimated by

$$D = \alpha V_s C_b \tag{16}$$

where $\alpha$ = a coefficient to be calibrated with experimental data, $C_b$ = near bed reference concentration.

## DEFINITION OF FLOW PARAMETERS

The turbulent cloud from the falling to the spreading stage is schematically shown in Fig.1, in which $W_0$ ($=A_0 \times \varepsilon_0 \times g$) is the initial total effective gravity force, $A_0$ is the initial total volume ($L \times M \times N$), $L$, $M$ and $N$ are the length, width and depth of the initial volume of suspension respectively, $h$ is the ambient water depth. $\varepsilon_0$ ($=(\rho-\rho_a)/\rho_a$) is the initial relative excess density, $z$ is the distance measured from the point of release to the centroid of the cloud, $H$ is the half width, $B$ is the average effective gravity force ($= W_0/A$), $A$ is the total volume and $V$ is the mass centre velocity of a cloud at $z$ in the falling stage. $x_f$ is the intrusion distance measured from the point of impingement, $H_g$ is the front height and $V_{fg}$ is the front propagating velocity and $B_g$ is the average effective gravity force of the cloud along $x_f$ in the spreading stage. $W_d$ is the effective gravity force of deposited particles. These parameters are non-dimensionalised as $H^* = H/(A_0^{1/3})$, $V^* = V/(W_0^{1/2}/A_0^{1/3})$, $B^* = B/(W_0/A_0)$, $z^* = z/(A_0^{1/3})$, $x_f^* = x_f/(A_o^{1/3})$, $H_g^* = H_g/(A_o^{1/3})$, $V_{fg}^* = V_{fg}/(W_0^{1/2}/A_o^{1/3})$, $B_g^* = B_g/(W_0/A_0)$ and $W_d^*$ ($= W_d/W_0$) respectively. $^*$ indicates the non-dimensional quantity.

## SENSITIVITY ANALYSIS

The value of Smagorinsky constant $C_s$ typically ranges from 0.07 to 0.27 (Murakami and Iizuka

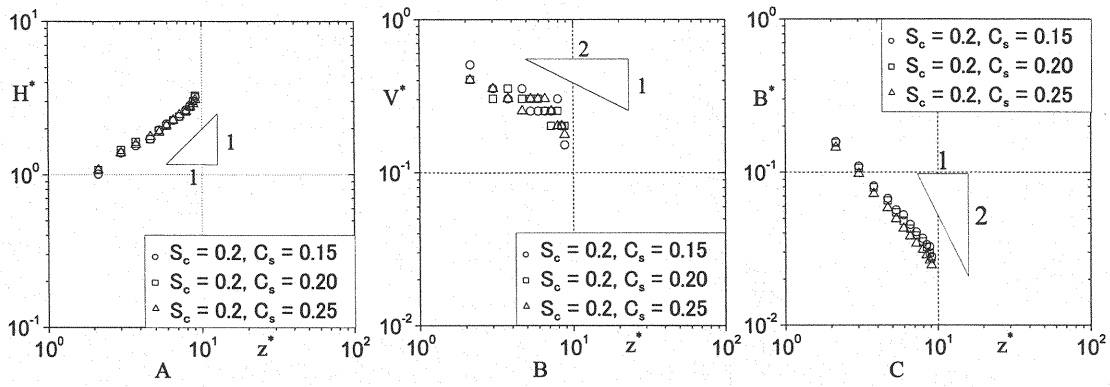


**Fig. 2** Sensitivity of $C_s$ on $H^*$, $V^*$ and $B^*$ with $S_c = 0.2$

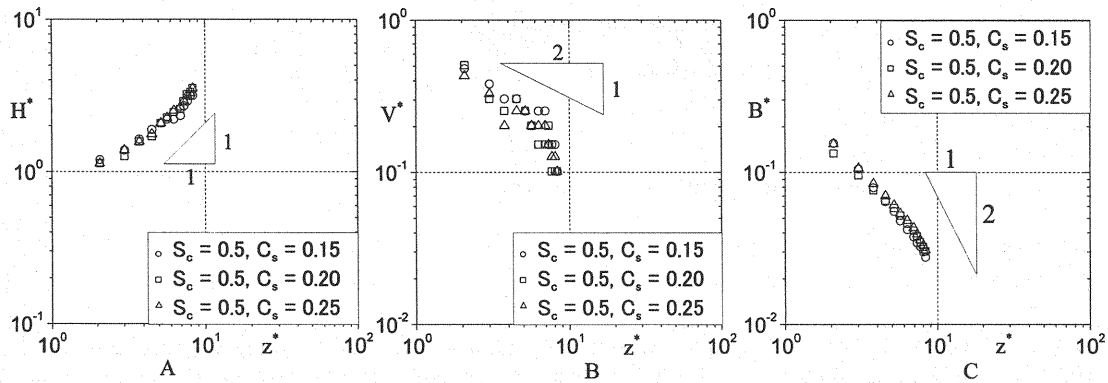


**Fig. 3** Sensitivity of $C_s$ on $H^*$, $V^*$ and $B^*$ with $S_c = 0.5$

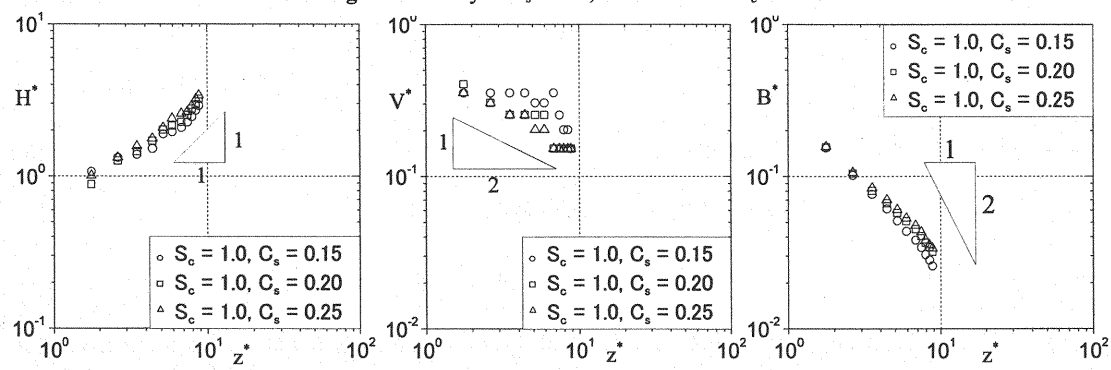


**Fig. 4** Sensitivity of $C_s$ on $H^*$, $V^*$ and $B^*$ with $S_c = 1.0$

(13)), while the value of Schmidt number $S_c$ for buoyancy induced flows is not yet known. The sensitivity of $C_s$ and $S_c$ to non-dimensional flow parameters as $H^*$, $V^*$ and $B^*$ is, therefore, examined using initial conditions of investigations as reported by Akiyama et al.(2). The value of constants are selected based on comparison with the two-dimensional particle thermal theory developed by Akiyama et al. (3), where such relationships as $H^* \propto z^*$, $B^* \propto z^{-2}$ and $V^* \propto z^{-1/2}$ are valid at least when the particle Reynolds number $R_p$ ($= d\, V_s/\nu$) is in the range of 0.06~6.0. In the analysis, the grid size is taken as $\Delta x = \Delta y = \Delta z = 1$ cm.

The cloud interface is defined as a point where the excess density of the cloud is 2% of the maximum relative excess density of the cloud. Figs. 2, 3 and 4 show the effect of $C_s$ and $S_c$ on $H^*$, $B^*$ and $V^*$. $C_s$ and $S_c$ were found to be insensitive to $H^*$ and $B^*$. However, the trend of $B^*$ is observed to

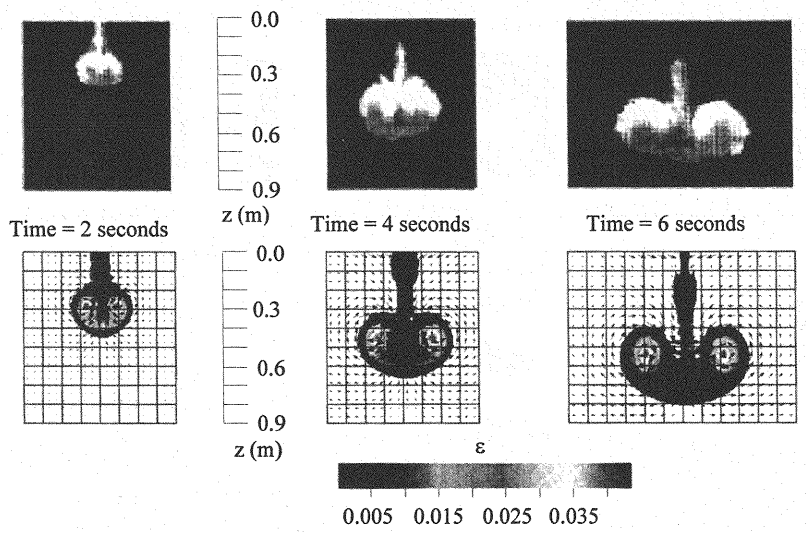


**Fig. 5** Comparison of experimental photographs and the simulated 2D cloud at different time interval in the falling stage.

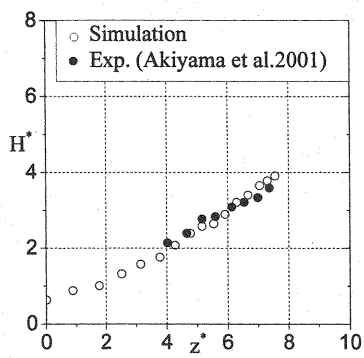


**Fig.6** The comparison of simulated and experimental $H^*$ for 2D cloud in the falling stage.

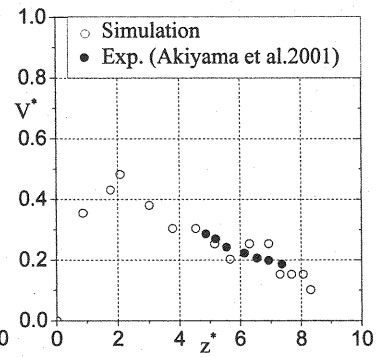


**Fig.7** The comparison of simulated and experimental $V^*$ for 2D cloud in the falling stage.

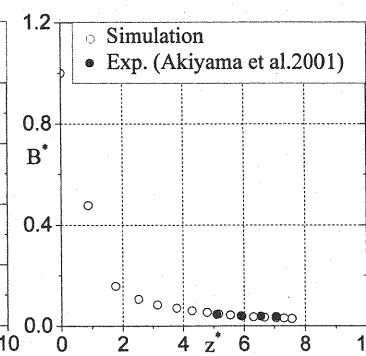


**Fig.8** The comparison of simulated and experimental $B^*$ for 2D cloud in the falling stage.

approach closer to that of the thermal theory as $S_c$ is increased to 1.0. The trend of simulated $V^*$ is found to be closest to that of thermal theory when the $C_s$ =0.25 and $S_c$ =1.0 as shown in Fig. 4b. Therefore, these values were selected as suitable values of model constants and used in the following computations.

## TWO-DIMENSIONAL PARTICLE CLOUD

A two-dimensional particle cloud from the falling to the spreading stage is simulated against experimental results as reported by Akiyama et al. (2). In the experiments, the suspension was a mixture of water and uniform glass beads with diameter $d$ = 0.0044cm and submerged specific gravity s =1.48. The initial volume of the suspension $A_0$ was 500 $cm^3$ and the initial relative density difference $\varepsilon_0$ was 0.194, so that the initial total effective gravity force $W_0$ was 95157 $cm^4/sec^2$. In the simulations, a computational domain of $951 \times 10 \times 91$ nodes and a uniform grid of size $\Delta x = \Delta y = \Delta z = 1$ cm is used. The initial volume of suspension is defined as $10 \times 10 \times 5$ nodes. A. The time step $\Delta t$ is 0.0025 second. The non-slip type boundary conditions taken on bottom and sides of the tank. The water surface is treated as slip-wall type boundary condition. Fig.5 shows the comparison of simulated cloud with the

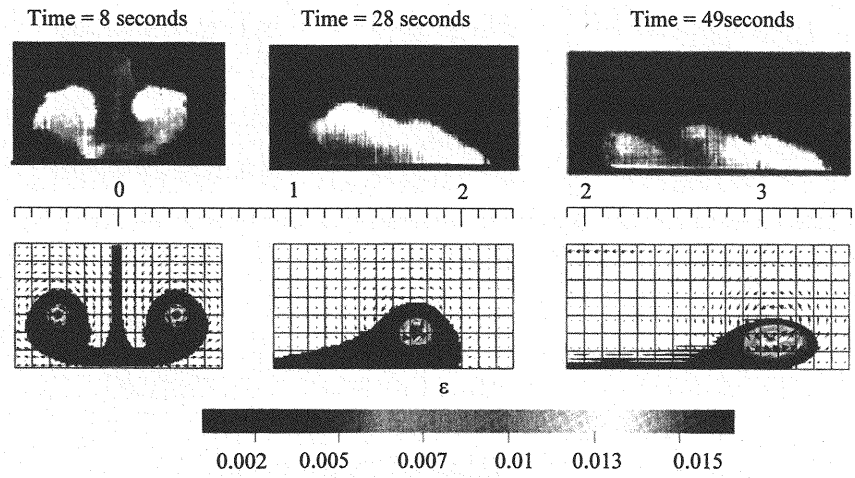


**Fig. 9** Comparison of experimental photographs and the simulated 2D cloud at different time interval in the spreading stage.

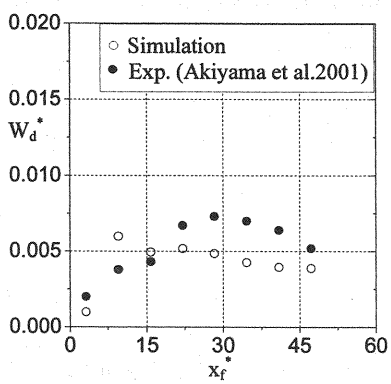


**Fig. 10** The comparison of simulated and experimental $W_d^*$ in two-dimensional cloud in the spreading stage.

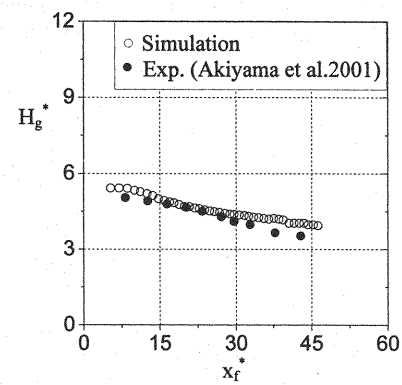


**Fig. 11** The comparison of simulated and experimental $H_g^*$ in two-dimensional cloud in the spreading stage.

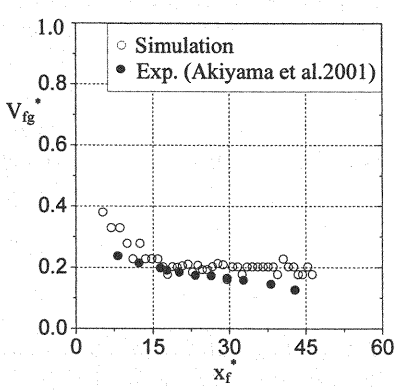


**Fig. 12** The comparison of simulated and experimental $V_{fg}^*$ in two-dimensional cloud in the spreading stage.

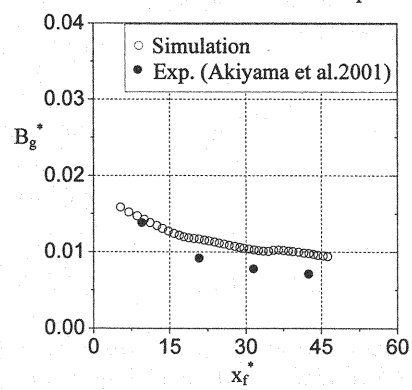


**Fig. 13** The comparison of simulated and experimental $B_g^*$ in two-dimensional cloud in the spreading stage.

experimental photographs at different time in the falling stage. In the figure the velocity vectors indicating internal circulatory motion are superimposed on the relative density difference contours. Soon after the release of suspension, a pair of vortexes is formed which are visible in experimental photographs and in simulation. The shape, size and position of the simulated cloud are in good agreement with the experimental photographs. Figs. 6-8 shows the comparison of simulated $H^*$, $V^*$ and

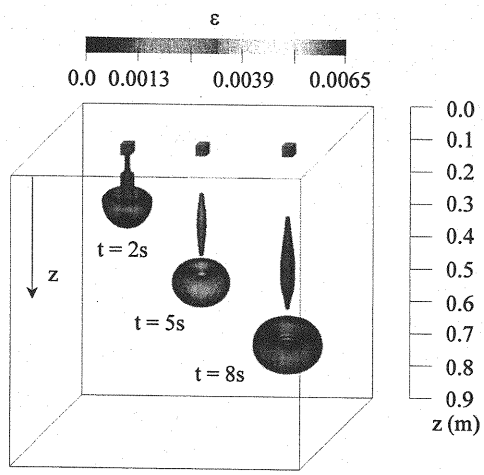


**Fig.14** Simulated axisymmetric cloud at 2, 5, and 8 seconds respectively in the falling stage.

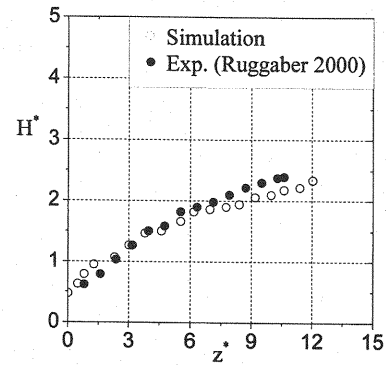


**Fig.15** The comparison of simulated and experimental $H^*$ in axisymmetric cloud in the falling stage.

$B^*$ with the experimental data. It was found that the model reproduces the motion of two-dimensional particle cloud in the falling stage to a reasonably good extent.

At the time of impingement of the falling cloud, the motion is highly turbulent and most of the particles remain in suspension. After impingement on the bottom, the two-dimensional cloud breaks into two parts and each propagating in opposite direction. Due to the slumping motion of particles in suspension, a gravity current is formed and spreads over the bottom, depositing sediments onto the bottom. Fig.9 shows a comparison of simulation and experimental photographs in the spreading stage. The position and the height of the cloud are in agreement with the experiments. The shape of the cloud in the later stage is somewhat different from that of experimental photographs. One of the probable reasons for this discrepancy may be that $\alpha$ in Eq. 16 is taken constant ($\alpha = 2$). In this study $\alpha$ is determined so as that the simulated profile of $W_d^*$ matches with the overall profile of $W_d^*$ obtained from experiments (Akiyama et al. (2)) as shown in Fig. 10.

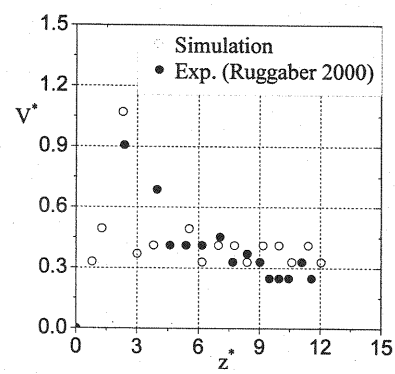


**Fig.16** The comparison of simulated and experimental $V^*$ in axisymmetric cloud in the falling stage.

Figs.11-13 show the comparison of simulated and experimentally observed $H_g^*$, $V_{fg}^*$, and $B_g^*$. It is observed from Fig.11 that $H_g^*$ decreases linearly with $x_f^*$. The model overestimated $H_g^*$ in the initial phase, but in later stage, i.e., from $x_f^*$=16, the model reproduced the $H_g^*$ to a reasonable accuracy. Fig.12 shows that the model slightly overestimated the $V_{fg}^*$ but the trend of simulation is similar as that of the experiments. Fig.13 reveals that $B_g^*$ decreases with $x_f^*$. The model reproduced $B_g^*$ quit well. The above comparisons demonstrate that the model is capable of simulating the complex dynamics process of the motion of particle cloud from the falling to spreading stage.

## AXISYMMETRIC PARTICLE CLOUD

The model was tested against the experimental results of the axisymmetric particle cloud in the falling stage, as reported by Ruggaber (17). In the experiments, the suspension was a mixture of water and uniform glass beads with diameter $d$ = 0.0024cm and was released below water surface. The initial

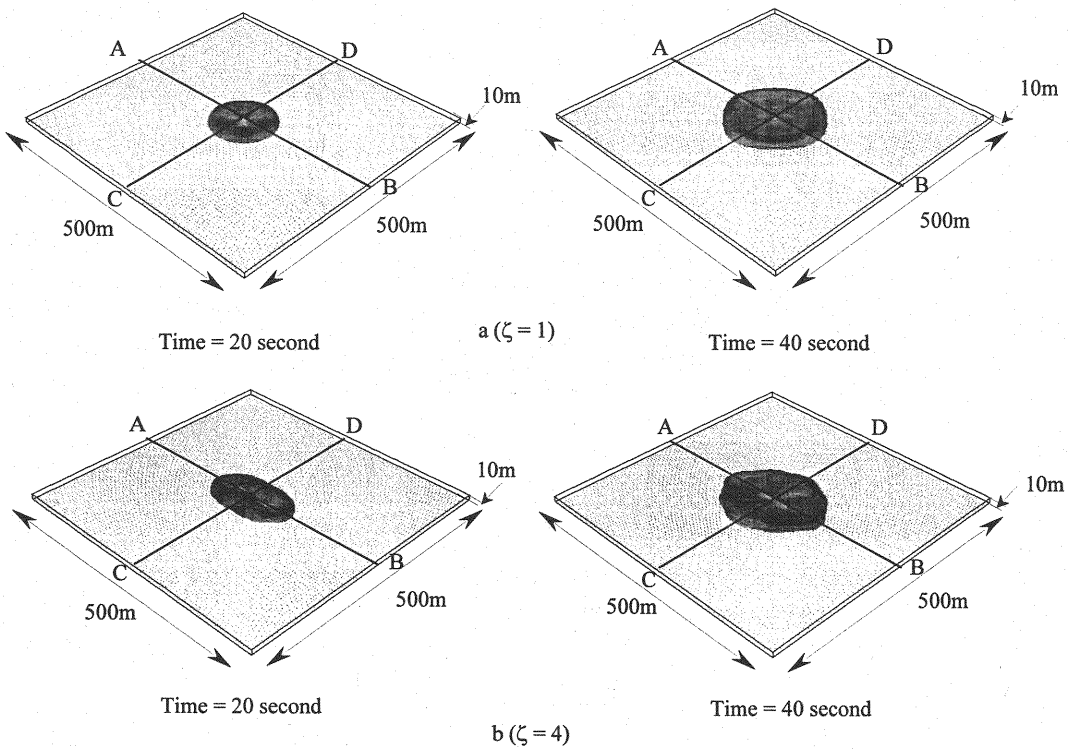


**Fig. 17** Isometric view of simulated particle cloud with $\zeta$=1 (above) and $\zeta$=4 (below) at different times in an ambient depth of 10 meters.

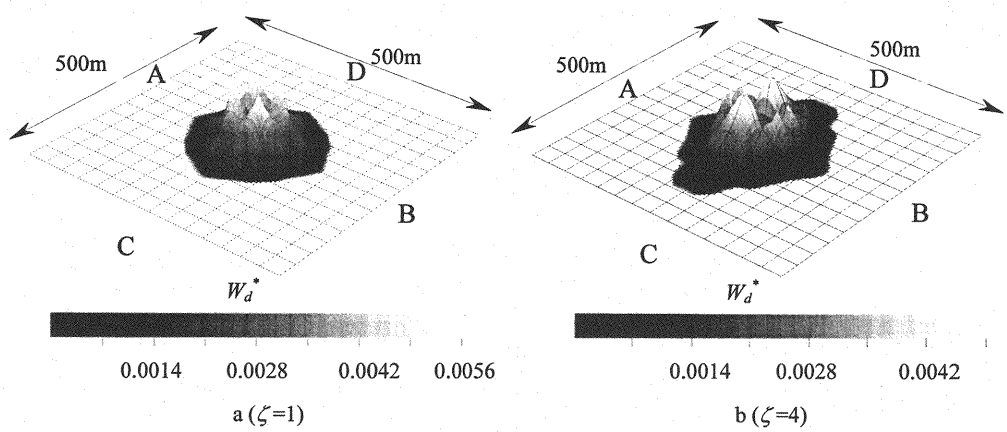


**Fig. 18** Distribution of simulated $W_d^*$ in case of 10 meter ambient depth.

volume of the suspension $A_0$ was 252 cm$^3$ and initial relative density difference $\varepsilon_0$ was 0.095 so that initial total effective gravity force $W_0$ is 23485.14 cm$^4$/sec$^2$. In the simulation a computational domain of 61×61×91 nodes is used. The size of the initial volume of the axisymmetric suspension is defined as 6×6×7 nodes. The grid size, time step, $C_s$ and $S_c$ are the same as the two-dimensional particle cloud simulations.

Fig.14 shows the simulated axisymmetric cloud. The shape of the axisymmetric cloud looks like an inverted mushroom, and soon after release, the particle cloud starts entraining ambient water and

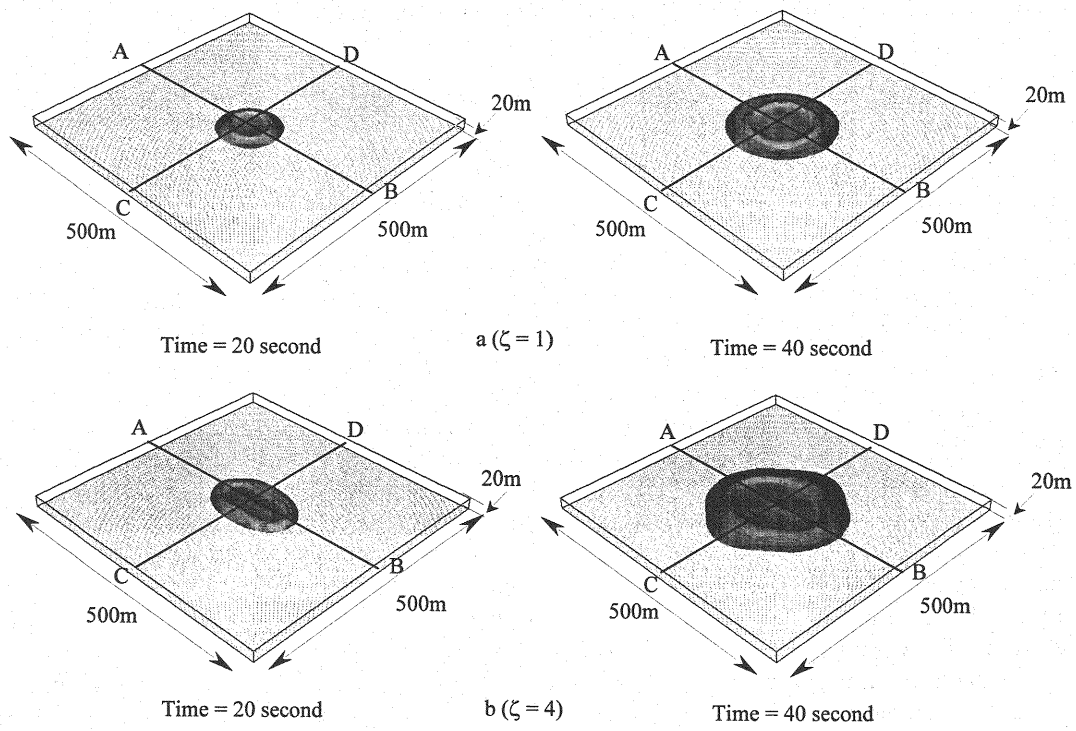


**Fig. 19** Isometric view of simulated particle cloud with $\zeta$=1 (above) and $\zeta$=4 (below) at different times in an ambient depth of 20 meters.

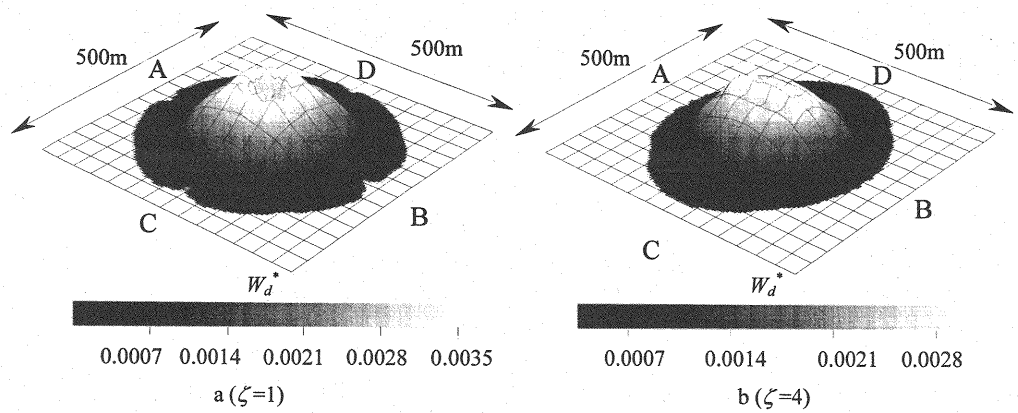


**Fig. 20** Distribution of simulated $W_d^*$ in case of 20 meter ambint depth.

hence grows in size. The cloud starts growing in a lateral direction and attains self-similar phase and forms a torus like structure. Fig.15 shows that the simulated $H^*$ is in reasonable agreement with the experimental results. Fig. 16 shows the comparison of simulated $V^*$ with the experiments. It was found that there is an initial accelerating flow regime which starts decelerating after reaching peak value at $z^* \approx 2.5$. The computed results agree quit well with the experiments. In the initial phase, the $H^*$ and $V^*$ are slightly over estimated in the simulation. This may be due to the difference in the way suspension was released. In the experiments, the suspension is released above the water surface, while, in

simulations, the suspension is introduced just below the water surface. Therefore, in the experiments, there is some initial velocity, while in the simulation initial velocity is set to zero.

## EFFECT OF AMBIENT WATER DEPTH AND INITIAL LENGTH TO WIDTH RATIO

Both the ambient water depth $h$ and the ratio $\zeta$ of initial length to initial width of suspension affect the behavior of the cloud to a great extent. Taking prototype scale conditions, the above validated model is used to investigate the effects of $h$ and $\zeta$ on such cloud characteristics as $W_d^*$, $H_g^*$ and $V_{fg}^*$. The simulation is carried out for a quiescent water body with dimensions of 500m length and 500m width, taking two cases of ambient water depth, i.e., $h$ =10m and 20m and two cases of ratio of initial length to initial width, i.e. $\zeta$=1 and 4. In the simulations the grid size of $\Delta x = \Delta z$ = 5m and $\Delta y$ = 1m is used. $\varepsilon_0$ and $d$ are taken as 0.297 and 0.1cm respectively. $A_0$ is kept constant as 12500 $m^3$ i.e., $A_0$ = 50 $\times$ 50 $\times$ 5 $m^3$ for $\zeta$=1 and 25 $\times$ 100 $\times$ 5 $m^3$ for $\zeta$ = 4 respectively.

Fig.17 shows an isometric view of the simulated cloud in shallower ambient water depth ($h$ = 10m) with $\zeta$=1 and $\zeta$ = 4. Fig. 18 shows the contours of effective gravity force of the deposited particles $W_d^*$ in shallower ambient water depth ($h$ = 10m) with $\zeta$=1 and $\zeta$ = 4. Figs.19 and 20 show these (isometric view and contours of $W_d^*$) in deeper ambient water depth ($h$ = 20m) with $\zeta$=1 and $\zeta$ = 4. The analysis is carried out along two mutually perpendicular sections, namely, AB and CD, which pass through the middle of the initial suspension. The suspension is introduced along the section AB for $\zeta$ = 4. The effects of $\zeta$ and $h$ on the cloud characteristics such as $H_g^*$, $V_{fg}^*$ and $W_d^*$ along the section AB and CD are presented in Figs. 21, 22 and 23 respectively.

In shallower ambient water depth, the particle cloud with $\zeta$=1 (Fig.17a), spreads in a similar way along the sections, while in case of a particle cloud with $\zeta$ = 4 (Fig.17b), the cloud development along the section CD becomes dominant. Fig.18 shows that particles tend to be deposited near the point of impingement. In case of $\zeta$=1 (Fig.18a) the particles deposit similarly along the sections, while in case of $\zeta$ = 4 (Fig.18b) more particles are deposited along the section CD than the section AB. Figs. 21-23 show that in case of $\zeta$=1, the behavior of $H_g^*$, $V_{fg}^*$ and $W_d^*$ along the section AB remains similar to that along the section CD.Fig.21 shows that in case of $\zeta$ = 4, $H_g^*$ decreases sharply along the section AB, while it remains almost constant after $x_f^* \approx 4.0$ along the section CD. Fig.22 shows that in case of $\zeta$ = 4, along the section AB (Fig.22a), $V_{fg}^*$ decreases faster and approaches to zero at $x_f^* \approx 5.2$, while along the section CD (Fig.22b), $V_{fg}^*$ remains larger and decreases slowly. Fig.23 shows that peak of $W_d^*$ in case of $\zeta$ = 1 is observed at $x_f^* \approx 1.0$ along both the sections, while in case of $\zeta$ = 4, peak is observed at the point of impingement along the section AB (Fig.23a) and at $x_f^* \approx 1.0$ along the section CD (Fig.23b).

In deeper ambient water depth, the cloud with $\zeta$=1 (Fig.19a), spreads similarly along the sections, while the cloud with $\zeta$ = 4 (Fig.19b) spreads more along the section CD. Fig.20 shows that particles tend to be deposited far from the point of impingement. In case of $\zeta$ =1 (Fig.20a), particles are deposited similarly along the sections, while in case of $\zeta$ = 4 (Fig.20b), the deposition pattern is affected by $\zeta$ in such a way that more particles are deposited along the section CD. Figs. 21-23 show that in case of $\zeta$ = 1, $H_g^*$, $V_{fg}^*$ and $W_d^*$ behave in a similar way along both the sections. In case of $\zeta$ = 4, along the section AB (Fig.21a), $H_g^*$ is observed to decrease sharply while along the section CD (Fig.21b), it falls slowly. Fig 22 shows that in case of $\zeta$ = 4 along the section AB (Fig.22a), $V_{fg}^*$ falls sharply and approaches to zero at $x_f^* \approx 5.5$. However, along the section CD (Fig.22b), $V_{fg}^*$ is observed to be significantly larger than that along the section AB. Fig.23 shows that in case of $\zeta$=1 along both the sections, the peak of $W_d^*$ is observed at $x_f^* \approx 2.5$. In case of $\zeta$ = 4, along the section AB (Fig.23a), the peak of $W_d^*$ is observed at the point of impingement while along the section CD (Fig.23b), it is observed at $x_f^* \approx 2.7$.

The above analysis shows that when the ambient water is deeper, the cloud in the thermal phase is more developed because the cloud remains longer in the falling stage, and at the time of impingement,

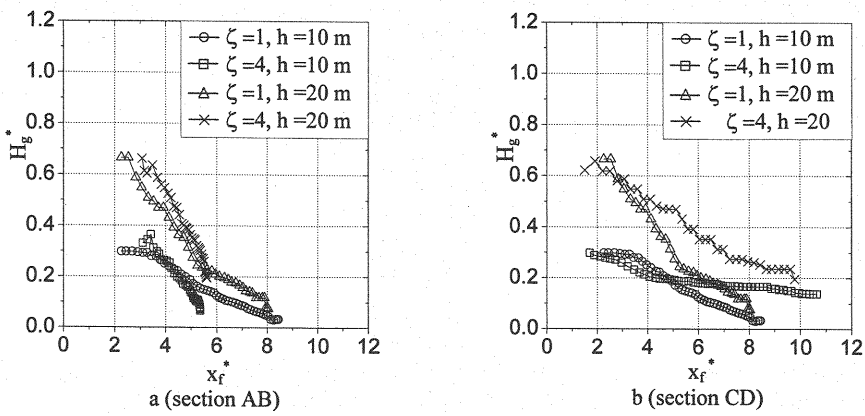


a (section AB) b (section CD)

**Fig. 21** The effect of ζ and *h* on $H_g^*$

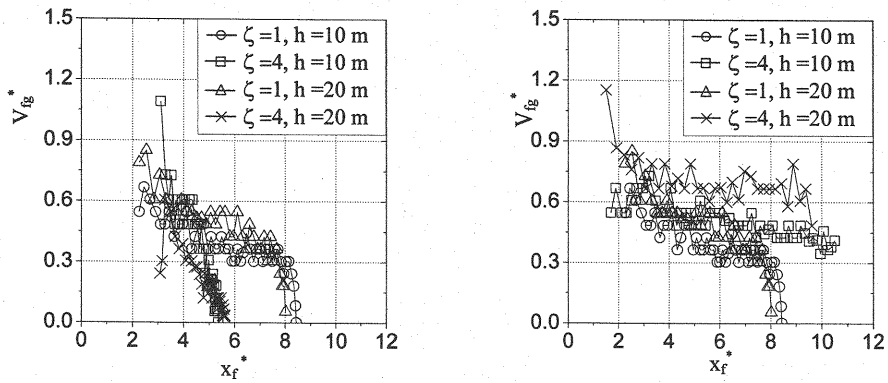


a (section AB) b (section CD)

**Fig. 22** The effect of ζ and *h* on $V_{fg}^*$

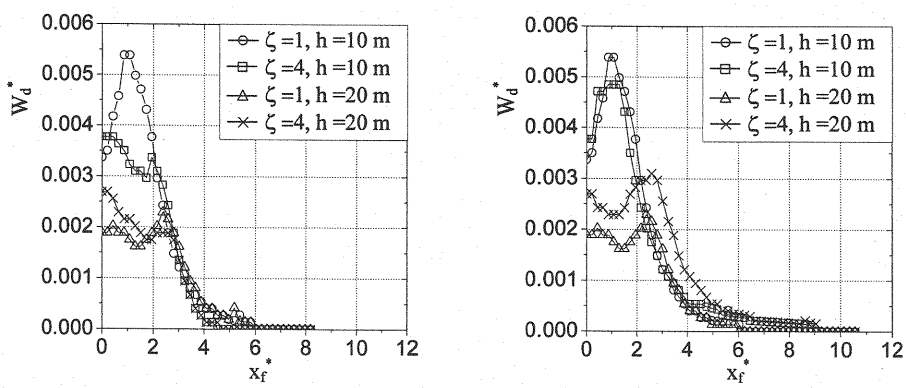


a (section AB) b (section CD)

**Fig. 23** The effect of ζ and *h* on $W_d^*$

the height of the cloud is higher. As a result, the stronger slumping motion is created and causes the turbidity to spread more over the bottom. Hence, the particles tend to be deposited away from the point of dumping. The effect of ζ on cloud characteristics like $H_g^*$, $V_{fg}^*$ and $W_d^*$ becomes weaker in deeper ambient water depth.

## CONCLUSION

A three-dimensional numerical model, using Large Eddy Simulation (LES), was developed for simulating the motion of particle clouds from the falling to spreading stage. In the model eddy viscosity is evaluated by means of the modified Smagorinsky model. The space derivatives are calculated by means of the fourth order accurate CFD scheme, and time derivatives are calculated by Crank Nicholson multi-step method. A sensitivity analysis is carried out to estimate appropriate values of Smagorinsky constant $C_s$ and Schmidt number $S_c$ to be used.

Findings show that the proposed model is capable of capturing the behavior of two-dimensional particle clouds from the falling to the spreading stage as well as the axisymmetric cloud in the falling stage, to a reasonable accuracy. The model is also applied to a prototype scale condition of direct dumping of sediments to investigate the effect of ambient depth and initial length to width ratio of the suspension on the subsequent motion of the particle cloud.

The model can be used to optimize the position and height of the turbidity fence used for control of the turbidity resulting from dumping of sediments.

## REFERENCES


1. Akiyama, J., Ura, M., Ying, X., Imamiya, M. and M. Suyama : Flow characteristics of dense cloud instantaneously released into quiescent fluid, Annual Journal of Hydraulic Engineering, JSCE, Vol.42, pp.529-534, 1998 (in Japanese).
2. Akiyama, J., Ying, X., and M. Shige-eda : Numerical simulation for dumped fine particles in quiescent water with finite depth, Journal of Hydraulic, Coastal and Environmental Engineering, JSCE, No.663/II-53, pp.43-53, 2001 (in Japanese).
3. Akiyama, J., Saiga, H., Singh, J., and M. Ura : Effect of water depth on the spread of a particle cloud produced by direct dumping, Annual Journal of Hydraulic Engineering, JSCE, Vol.47, pp.1141-1146, 2003 (in Japanese).
4. Baines, W.D. and E.J. Hopfinger : Clouds with large density difference, Journal of Atmospheric Environment, Vol.18, No.6, pp.1051-1057, 1984.
5. Buhler, J. and D.A. Papantoniou : Swarms of coarse particle falling through a fluid, Environmental Hydraulics, Lee & Cheung (eds), Balkerma, Rotterdam, pp. 137-140, 1991.
6. Bush, J.W.M., Thurber, B.A. and F. Blanchette : Particle clouds in homogeneous and stratified environments, Journal of Fluid Mech., Vol.489, pp.29-54, 2003.
7. Edison, T.M.: Numerical simulation of the turbulent Rayleigh-Benard problem using sub-grid modeling, Journal of Fluid Mech., Vol.158, pp.245-268, 1985.
8. Jiang, Q., Kunisu, H. and A. Watanabe : Numerical simulation of settling-dispersion processes of dredged material disposed from barges, Proceedings of Coastal Engineering, JSCE, Vol.44, pp.1031-1035, 1997 (in Japanese).
9. Lele, S.K. : Compact finite difference schemes with spectral-like resolution, Journal of Computational Physics, Vol.103, pp.16-42, 1992.
10. Li, C.W. : Convection of particle clouds, Journal of Hydraulic Research, IAHR, Vol.35, No.3, pp.363-376, 1997.
11. Li, C.W. and F. Zang : Three-dimensional simulation of clouds using a split operator scheme, International Journal of Numerical Methods in Heat and Fluid Flow, Vol.6, No.2, pp.23-35, 1996.
12. Maxworthy, T. : Turbulent vortex rings, Journal of Fluid Mech., Vol.64, part2, pp.227-239, 1974.
13. Murakami, S. and S. Iizuka : CFD analysis of turbulent flow past square cylinder using dynamic LES, Journal of Fluids and Structures, Vol.13, pp.1097-1112, 1999.
14. Nadaoka, K., Nihei, Y. and H. Yagi : An LES modeling for solid-fluid phase turbulent flow based on new formulation of solid-particle motion, , Journal of Hydraulic, Coastal and Environmental Engineering, JSCE, No.533/II-34, pp.61-73, 1996 (in Japanese).

15. Noh, Y. and H.J.S. Fernando : The transition in the sedimentation pattern of a particle cloud, Phys. Fluid, A5(12), pp.3049-3055, 1993.
16. Rahimipour, H. and D. Wilkinson : Dynamic behavior of particle clouds, Proceeding of 11th Australian Fluid Mechanics Conference, University of Tasmania, Hobart, Australia, 14-18, pp. 743-746, 1992.
17. Ruggaber, G.J. : Dynamics of particle clouds related to open-water sediment disposal, Ph.D. thesis, Massachusetts Institute of Technology, USA, 2000.
18. Snider, D.M. : An incompressible three-dimensional multiphase particle-in-cell- model for dense particle flows, Journal of computational physics, 170, pp.523-549,2001.
19. Tamai, M. and K. Muraoka : Numerical simulation on characteristics of turbidity transport generated in direct dumping of soil, Annual Journal of Hydraulic Engineering, JSCE, Vol. 42, pp.541-546, 1998 (in Japanese).
20. Tamai, M., Koji, M. and M. Akira : Study on falling behavior of a swarm of solid particles and induced flow field, Journal of Hydraulic, Coastal and Environmental Engineering, JSCE, No.509/II-30, pp.143-154, 1995 (in Japanese).
21. Ying, X., Akiyama, J. and M. Ura : Numerical investigation on the motion of 2-D particle clouds, Annual Journal of Hydraulic Engineering, JSCE, Vol.44, pp.1239-1244, 2000.

## APPENDIX- NOTATION

The following symbols are used in this paper:

$A_0$ = initial volume of particle suspension;
$A$ = volume of particle cloud at falling distance z;
$B$ = effective gravity force in the falling stage;
$B_g$ = average effective gravity force in spreading stage;
$c$ = sub-grid component of concentration;
$C$ = volumetric concentration of particles;
$C_b$ = near bed reference concentration;
$C_s$ = Smagorinsky constant;
$d$ = particle diameter;
$D$ = net deposition rate;
$g$ = acceleration due to gravity;
$h$ = total depth of ambient water;
$H$ = half width of cloud in the falling stage;
$H_g$ = front height in spreading stage;
$k$ = turbulent kinetic energy;
$L$ = length of initial cloud fluid;
$M$ = width of initial cloud fluid;
$N$ = depth of initial cloud fluid;
$P$ = pressure in excess of hydrostatic pressure at reference density;
$s$ = submerged specific gravity of particle;
$|\overline{S}|$ = magnitude of large-scale strain rate tensor;
$u'_l$ = sub-grid velocity component in $x_l$ direction;
$U_l$ = grid scale velocity component in $x_l$ direction;
$\overline{u'_l u'_m}$ = sub-grid correlation term between unresolved velocities;
$\overline{u'_l c'}$ = sub-grid correlation terms between sub-grid velocity and sub-grid concentration;
$S_c$ = Schmidt number;
$S_{ct}$ = turbulent Schmidt number;
$V$ = mass center velocity in the falling stage;

$V_{fg}$ = front propagation speed in the spreading stage;
$V_s$ = settling velocity of a particle;
$W_0$ = initial total effective gravity force;
$W_d$ = effective gravity force of deposited particles;
$x_f$ = intrusion distance in the spreading stage;
$z$ = depth of centroid of cloud in the falling stage measured from water surface;
$H^*$, $V^*$, $B^*$, $z^*$, $x_f^*$, $H_g^*$, $V_{fg}^*$, $B_g^*$, $W_d^*$ = Non-dimensional form of H, V, B, z, $x_f$, $H_g$, $V_{fg}$, $B_g$, and $W_d$.
$\alpha$ = empirical coefficient for particle deposition flux;
$\Delta$ = filter width;
$\Delta t$ = time step;
$\Delta x$, $\Delta y$, $\Delta z$ = grid size in $x$,$y$, and $z$ direction;
$\delta_{ij}$ = kronecker delta function;
$\varepsilon_0$ = initial relative excess density;
$\varepsilon$ = relative density difference;
$\phi$ = ratio of initial depth to width of suspension (N/M);
$\rho$ = density of cloud fluid;
$\rho_a$ = density of ambient fluid;
$\Delta\rho$ = density difference $(\rho-\rho_a)$;
$\nu$ = kinetmatic viscosity;
$\nu_t$ = sub-grid scale eddy viscosity; and
$\zeta$ = ratio of initial length to width of suspension (L/M), respectively.

(Received July 25, 2005 ; revised September 20, 2005)